Enhancing the acidic oxygen evolution reaction efficiency of sol–gel synthesized $SrCo_{0.5}Ir_{0.5}O_3$ catalysts through optimized ball milling and acid leaching

Cite as: APL Energy 3, 016101 (2025); doi: 10.1063/5.0242496
Submitted: 4 October 2024 • Accepted: 28 December 2024 •
Published Online: 13 January 2025

Dongqi Yang,[1] Nicolai Andreas,[1] Ankit K. Yadav,[2] Kyriakos C. Stylianou,[2] and Zhenxing Feng[1,a)]

AFFILIATIONS

[1] School of Chemical, Biological and Environmental Engineering, Oregon State University, Corvallis, Oregon 97331, USA
[2] Materials Discovery Laboratory, Department of Chemistry, Oregon State University, Corvallis, Oregon 97331, USA

Note: This paper is part of the Special Topic on Energy Materials for Extreme Environments.
[a)] **Author to whom correspondence should be addressed:** zhenxing.feng@oregonstate.edu

ABSTRACT

High-efficiency and low-cost catalysts for the oxygen evolution reaction (OER) in acidic electrolytes are critical for electrochemical water splitting in proton exchange membrane (PEM) electrolyzers to produce green hydrogen, a clean fuel for sustainable energy conversion and storage. Among OER catalysts, solid-state synthesized $SrCo_{1-x}Ir_xO_3$ has demonstrated superior activity compared to commercial standards, such as IrO_2 and RuO_2. However, the solid-state synthesis process is economically inefficient for industrial use due to the potential for impurities and low yield of the final product. In addition, the requirement for electrochemical cycling to activate the catalyst introduces contaminations and uncertainties for industrial applications. In this study, a modified solution-based sol–gel method was employed to produce $SrCo_{0.5}Ir_{0.5}O_3$ (SCIO) with high purity and yield. Subsequent ball milling and acid leaching treatments were applied, resulting in a catalyst with higher efficiency than those activated solely by electrochemical cycling. The electrochemical analysis and physical characterizations of our SCIO catalyst after *ex-situ* post-synthesis treatments show a similar active phase in composition and structure to those obtained through *in situ* electrochemical cycling and activation. Our approach simplifies the preparation process, making the catalyst ready for direct use in PEM electrolyzers without further treatment, offering a promising solution for producing high-performance, industrial-scale OER catalysts.

I. INTRODUCTION

Producing clean fuels by converting and storing renewable energy into molecular bonds such as hydrogen (H_2) is imperative in combating societal and environmental issues, such as climate change, air pollution, limited resources leading to energy insecurity, and economic instability.[1–4] Electrolyzers are a vital tool to ensure such processes by splitting water using electricity generated from renewable energy sources (e.g., solar, wind) to green hydrogen.[3] The high efficiency and ability to operate at high current densities, along with a compact design, make proton exchange membrane (PEM) electrolyzers one of the most favored choices (e.g., compared to alkaline electrolyzers) for green H_2 production. In addition, they are well-suited for integration with intermittent renewable energy sources, such as wind and solar.[5,6] However, the H_2 production cost from PEM electrolyzers is relatively high (~$5/kg), mainly due to the use of expensive, precious metals, such as iridium (Ir) and platinum (Pt), in the anode and cathode, respectively.[7,8] In addition, the acidic condition in which PEM electrolyzers operate corrodes the materials, leading to low durability of the device. Under optimistic projections, achieving H_2 production costs below $1/kg by 2031 (a goal set by the U.S. Department of Energy) depends on significant reductions in capital costs and the effective utilization of regional renewable energy potentials.[9] In particular, for PEM electrolyzers, the main challenge lies in addressing the slow reaction kinetics and the reliance on expensive precious metals, such as iridium (Ir), for

the oxygen evolution reaction (OER) at the anode. Overcoming these challenges is crucial for enhancing the efficiency and economic viability of PEM electrolyzers, making them a more cost-effective solution for hydrogen production.[10]

Currently, commercially ready electrocatalysts used for OER are ruthenium- or iridium-based.[11–13] Although ruthenium-based catalysts exhibit higher initial activity for OER, iridium-based catalysts provide significantly greater stability under acidic conditions.[14] The enhanced stability makes iridium-based catalysts more suitable for long-term use in acidic environments and better prepared for applications in PEM electrolyzers and fuel cells.[13,15] In 2016, Seitz *et al.*[12] demonstrated an innovative $IrO_x/SrIrO_3$ catalyst that has high activity for OER in acidic environments. It was hypothesized that strontium (Sr) completely leached out from strontium iridium oxide ($SrIrO_3$) catalyst top layers in electrochemical cycling, thus forming a highly active surface that makes the catalyst achieve an overpotential of 270–290 mV at 10 mA/cm^2_{oxide} (normalized to the catalyst surface area) for over 30 hours. Later, Wan *et al.*[16] used smooth, epitaxial $SrIrO_3$ thin films as a model system and combined multimodal surface-sensitive x-ray characterizations with density functional theory (DFT) to show that a highly disordered Ir octahedral network with Ir square-planar motifs is the final active phase that is induced by the partial leaching of Sr from the surface during the electrochemical cycling. Furthermore, Chen *et al.*[17] successfully synthesized a micrometer-level cobalt-doped $SrIrO_3$ catalyst, $SrCo_{0.5}Ir_{0.5}O_3$ (SCIO), in powder form via a solid-state synthesis method and demonstrated the restructured and electrochemically activated honeycomb-like IrO_xH_y phase, similar to what Wan *et al.* showed, with comparable OER performance as $SrIrO_3$ thin film catalysts under acidic conditions but with 50% reduced iridium usage.[12,16,18] Although these works provided a deep mechanistic understanding and moved toward more applied research, the solid-state synthesis approach presented notable drawbacks, including the presence of impurities, significant yield losses, and the production of large particle sizes. Moreover, the necessity for additional electrochemical activation hindered the catalyst's commercial viability.

To address these challenges, a solution-based sol–gel synthesis is developed in this work. This facile method offers the potential for higher yield and purity, thereby mitigating the issue of impurities associated with the solid-state method. Furthermore, post-synthesis processes such as ball milling and acid leaching are introduced to reduce the particle size down to hundreds of nanometers and activate the material without requiring further electrochemical treatments. These refinements aim to enhance the catalyst's surface area and reactivity, facilitating its practical application in acidic OER environments of commercial PEM electrolyzers. In this article, we also discuss the optimization of synthesis conditions and subsequent treatments to enhance cobalt mobilization and iridium exposure, ultimately improving the performance and commercial feasibility of SCIO. Our synthesized and pre-activated SCIO catalyst exhibits a lower OER overpotential (221 mV to reach 10 mA/cm^2_{geo} in 1M $HClO_4$), higher mass activity (1.47 $A/mg_{Ir\ ECSA}$ in 1M $HClO_4$), and a better Tafel slope (35.1 mV/dec in 1M $HClO_4$) compared to those previously reported for $SrIrO_3$-based catalysts and commercial super-high-surface-area TKK IrO_2 standards under the same perchloric acid ($HClO_4$) electrolyte conditions.[12,17,19,20]

II. METHOD

A. Synthesis

A sol–gel synthesis method was meticulously developed for the preparation of pseudo-cubic SCIO. Citric acid was employed as a stabilizing agent, while ethylenediaminetetraacetic acid (EDTA) served as a chelating agent. Various ratios of metal to EDTA to citric acid were evaluated, and the optimal ratio was determined to be 1:1:1.5. Ammonium hydroxide was introduced to facilitate the hydrolysis reaction with EDTA. The pH was carefully adjusted using nitric acid to maintain an acidic environment with a pH below 3, which is critical for smooth gelation and the production of fine particle sizes. The gelation process was allowed to proceed over a 12-h period. Subsequently, the gel was dried at 150 °C in air for a minimum of 4 h to eliminate impurities, with additional drying performed as necessary to achieve a fully interlinked dry gel. The dried gel was finely ground and then subjected to calcination at 1150 °C for 12 h, with a controlled heating rate of 4 °C/min, using a Sentro Tech Corp 1200 °C muffle box furnace. After naturally cooling back to room temperature, the sample was ground using an agate mortar and collected for further analysis.

B. Post-synthesis treatment

To reduce the SCIO particle size and increase the surface area, the sample underwent ball milling. Acid leaching was subsequently performed to *ex-situ* activate the SCIO catalyst as the alternative method for *in situ* electrochemical cycling used in previous reports.[12,16,17,19] Optimal conditions were determined as shown in Fig. S1 for ball milling time and Fig. S2 for acid leaching conditions. The best condition was determined as ball milling for 24 h, followed by leaching in 1M $HClO_4$ for 5 h. The optimized procedures of synthesis and post-synthesis treatments are illustrated in Fig. 1.

C. Optimization

The optimal acid concentration for leaching was determined through a series of experiments. Initially, 0.1M perchloric acid was used, following the method of Chen *et al.*, but it proved insufficient (e.g., low activity) for activation under *ex-situ* conditions. Concentrations increased to 0.5M, 0.7M, and 1M, with the best results obtained using 1M acid. Homogeneous soaking methods, including stirring and ultrasonic waves, were also evaluated, with stirring proving slightly more efficient. Tests conducted at 30 °C showed that the ultrasonic method improved penetration but was less effective overall than stirring. To improve the catalytic performance of SCIO, the sequence of ball milling followed by acid leaching was adopted, with 12 h of milling and 5 h of leaching yielding optimal results at higher acid concentrations, namely the best stability and activity. Our optimization processes show that longer durations of acidic leaching led to excessive removal of cobalt and strontium, compromising structural stability, while shorter durations struck a balance between activity and stability. Higher acid concentrations (2M, 5M, and 8M) were tested, too, but did not outperform 1M perchloric acid, confirming that 1M was the optimal choice. Efforts to reduce particle size below 500 nm through ball milling were partially successful. Despite 72 h of milling, some particles remained over 2 μm. Extended milling disrupted the Sr and Co structures,

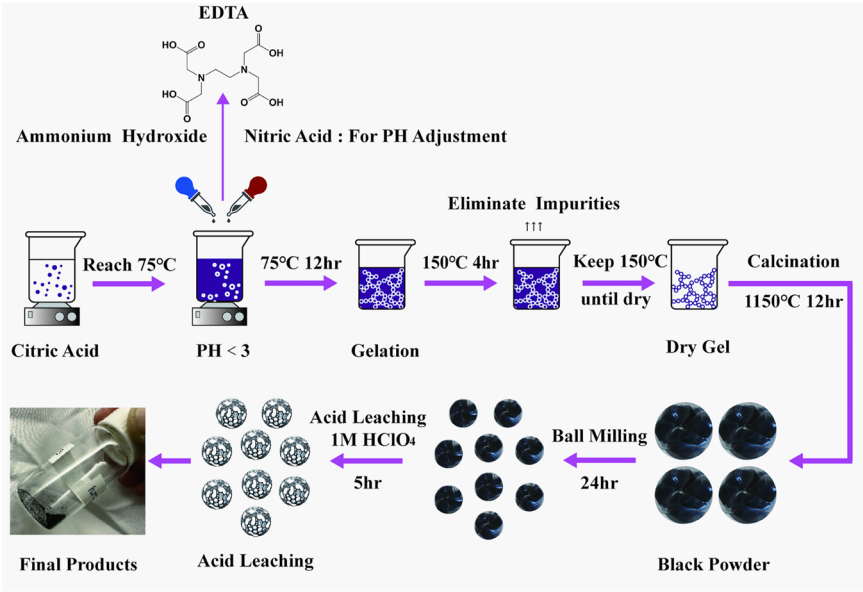

FIG. 1. Synthesis scheme of SCIO synthesized utilizing the sol–gel methodology with post-synthesis treatment to attain a high efficiency final product.

as the SEM analysis revealed, leading to instability during testing. This instability was linked to sample detachment from the carbon disk, resulting in a poor oxygen evolution reaction (OER) performance under acidic conditions. The findings highlight the need to balance particle size reduction with maintaining structural integrity for efficient post-processing.

D. Characterization

X-ray diffraction (XRD) analysis was utilized to confirm the sample's purity and crystallinity, using a Rigaku SmartLab diffractometer with a Mo source and a 1D line detector operating on a flat plate configuration with a 5 mm slit. Scanning electron microscopy (SEM) was conducted using an FEI Quanta 3D dual-beam SEM-FIB, which provided insights into the particle size and elemental composition. X-ray fluorescence (XRF) measurements were taken at the X-Ray Analytical Facility at the University of Oregon using a Rigaku ZSX Primus IV. Powder samples were loaded onto a crucible and covered tightly in shrink wrap before being placed into the tool. The measured data were analyzed using the Python package scipy.integrate in order to get elemental counts. X-ray photoelectron spectroscopy (XPS) was performed using a ThermoScientific ESCALAB 250 at the Surface Analysis Facility at the Center for Advanced Materials Characterization in Oregon (CAMCOR) at the University of Oregon and a PHI 5600 XPS at Oregon State University to gather detailed information on the chemical environment of the sample. The XPS is done under an Al K alpha source with a step size of 0.1 or 0.2 eV. The scan rate was varied from sample to sample. Nitrogen adsorption–desorption isotherms were measured at 77 K using a Micromeritics 3FLEX adsorption analyzer. Before the measurement, the samples were activated at 120 °C for 20 h under vacuum to remove residual solvent molecules within the structure. The Brunauer–Emmett–Teller (BET) surface areas were determined using the BET model.[21,22]

E. Electrochemical Tests

Catalyst ink was prepared by grinding 2.5 mg of the SCIO catalyst with 1 mg of carbon (C65), followed by air drying at 80 °C for 4 h. Subsequently, 375 μl of water, 112.5 μl of isopropanol, and 12.5 μl of Nafion were added to the dried mixture, which was then sonicated for at least 1 h until the sample was fully dispersed. A 10 μl aliquot of the catalyst ink was deposited onto a glassy carbon disk to achieve a catalyst loading of 0.05 mg. Cyclic voltammetry (CV) tests were conducted under nitrogen flow at 1600 rpm in 0.1M $HClO_4$ across a voltage range of 1.161–1.461 V in a three-electrode system. A double junction silver chloride (Ag/AgCl) electrode was used as the reference electrode, and a platinum wire served as the counter electrode. To obtain the Tafel slope, chronoamperometry measurements were performed in steps of 10 mV, where a relaxation time of 60 seconds is used for each step to allow the current to achieve a steady state.[18] All OER measurements were performed using a Cortest CS2350 biopotentiostat coupled with a modulated speed rotator (Pine Research Instrumentation).

III. RESULTS AND DISCUSSION

The SCIO synthesized via the sol–gel method was confirmed to exhibit high phase purity through XRD analysis, as shown in Fig. 2(a). SEM images, depicted in Figs. 2(b) and 2(c), revealed that the particles synthesized using the sol–gel method had an average size of ~2.11 μm, indicating relatively large particle dimensions (see the particle distribution analysis in Fig. S4). The element ratios were analyzed using energy dispersive x-ray (EDX) (Table S1), x-ray photoelectron spectroscopy (XPS) (Table S6), and x-ray fluorescence (XRF) (Table S7), showing that the composition closely matches the nominal value of $SrCo_{0.5}Ir_{0.5}O_3$. Subsequently, ball milling and acid leaching were conducted, with the optimal conditions to achieve the best electrochemical performance determined, as shown in Figs. S1 and S2, respectively. Following ball

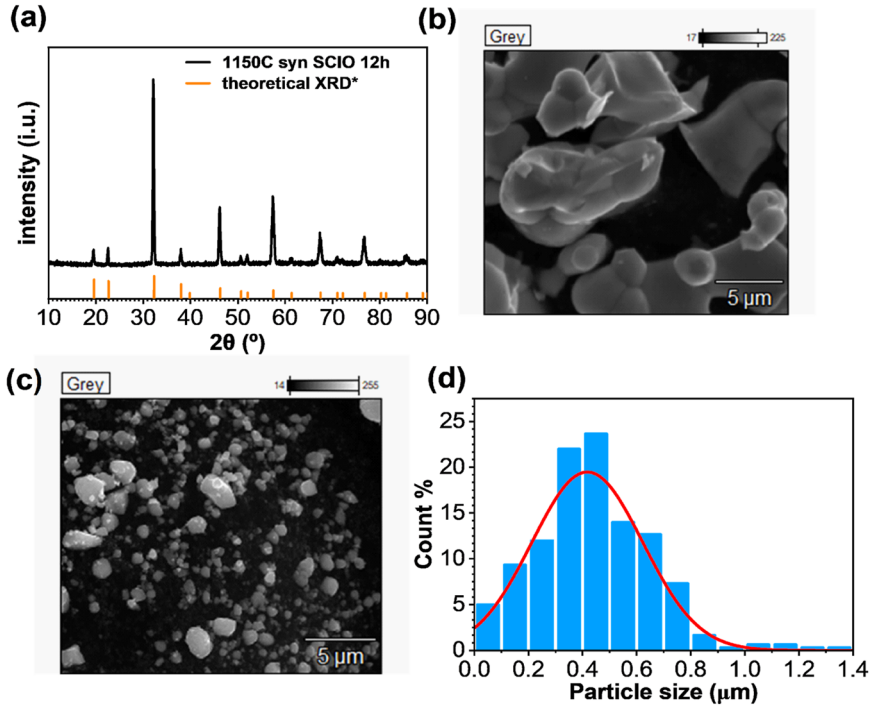

FIG. 2. (a) XRD of SCIO synthesized with the sol–gel method compared to the reference XRD spectrum of SCIO synthesized with the solid-state method from Chen *et al.*[17] (b) SEM images of the SCIO pristine sample synthesized by the sol–gel method (SCIO-SG) and (c) SEM images of SCIO synthesized by the sol–gel method after ball milling and acid leaching processing (SCIO-SG-P). (d) Particle size distribution plot of sol–gel synthesized SCIO after ball milling for 24 h and acid leaching for 5 h.

milling for 24 h and subsequent acid leaching for 5 h, a significant reduction in particle size was observed. The ball-milled and acid-leached samples were analyzed using XRD, revealing the same phase (Fig. S3). The decrease in diffraction intensity and the broadening of the XRD peak widths indicate a reduction in particle size. However, this reduction was not uniform, as some large particles remained. As illustrated in Fig. 2(d), the average particle size was found to be ~461 nm, with the majority of particles exhibiting diameters in the range of 400–500 nm. In addition, the crystalline domain size of our samples after post-synthesis treatments was estimated using Debye Scherrer's equation to be 123.4 nm (see the supplementary material for more details), which is smaller than the averaged 461 nm overall particle size measured by SEM. This suggests that amorphous structures existed in these particles, probably dominating on the outer surfaces due to the *ex-situ* acid leaching from the post-synthesis treatment. The elemental ratios of the SCIO sample after post-synthesis treatment were analyzed using EDX (Table S1), showing a reduction in Sr, Co, and O concentrations and thus forming a Sr- and Co-deficient SCIO composition. Further XPS analysis (Table S6; Figs. S5–S7) on SCIO synthesized from solid-state and sol–gel methods and corresponding treatments (i.e., *in situ* activation and post-synthesis treatment) also confirms the leaching of Sr and Co with Sr- and Co-deficient compositions. These results also match the structure and composition of $SrIrO_3$-based catalysts after electrochemical cycling from Chen *et al.* and Seitz *et al.*,[12,17] suggesting that our SCIO samples, after the optimized synthesis and post-synthesis treatment procedures, are similar to the final active phases obtained in previously reported *in situ* electrochemical activation.

To understand the chemical effects on SCIO samples through ball milling and acid leaching processes, XPS measurements were carried out on pristine SCIO synthesized by the sol–gel method (SCIO-SG) and the SCIO synthesized by the sol–gel method after ball milling and acid leaching processes (SCIO-SG-P). The EDX analysis above showed that the SCIO-SG sample has a slight oxygen deficiency, resulting in a composition approximated as $SrCo_{0.5}Ir_{0.5}O_{2.75}$. A subsequent XPS analysis revealed that iridium is present in mixed oxidation states of +4 and +5, while cobalt exhibits +2 and +3 oxidation states, as shown in Figs. 3(a) and 3(b), consistent with the expected chemical states in the composition calculated from the EDX analysis. In contrast, the $Ir^{3+}/^{4+}$ was identified in the Ir 4f XPS spectra of SCIO-SG-P, in addition to $Ir^{4+}/^{5+}$, suggesting that the post-synthesis treatment processes induce a shift in iridium's oxidation states, with Ir partially reduced to the 3+ and 4+ states. The combined EDX and XPS data for the post-synthesis treated SCIO sample suggested the existence of a mixed composition in SCIO-SG-P, for example, $Sr_{0.3}Co_{0.3}Ir_{0.7}O_{2.15}$ (with Ir^{4+}) and $Sr_{0.3}Co_{0.3}Ir_{0.7}O_{1.8}$ (with Ir^{3+}). Interestingly, the EDX results indicate a higher overall oxygen content, possibly because EDX captures the bulk oxygen composition, whereas XPS is more surface-sensitive, detecting potential differences in surface chemistry. Furthermore, ambient oxygen may occupy vacancies at the catalyst's surface, further contributing to these different observations.

In addition, cobalt appears to be converted entirely to Co^{3+} after post-synthesis treatment processes [Fig. 3(b)]. This can be attributed to the dissolution of cobalt from the acid leaching step. Acid leaching might preferentially remove Co^{2+} species that are not strongly bound to the material because Co^{2+} has a more stable

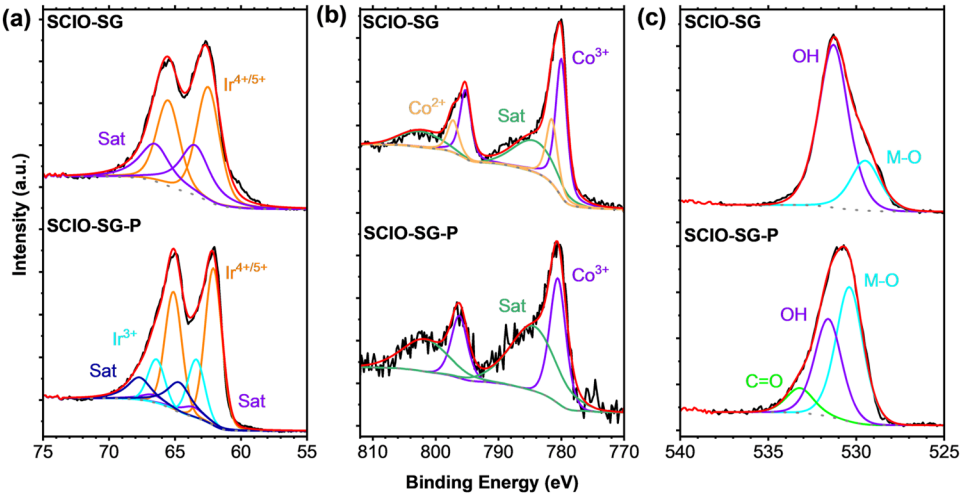

FIG. 3. XPS analysis of SCIO-SG and SCIO-SG-P: (a) Ir 4f, (b) Co 2p, and (c) O 1 s.

octahedral coordination with ligands such as water.[23] It exhibits higher solubility under acidic conditions and is removed during acid leaching. In contrast, the Co^{3+} forms insoluble oxides or remains bound in the crystal structure. As Co is leached from the surface, the remaining iridium becomes more exposed with mixed Ir^{3+} and Ir^{4+} that are much more stable under acidic conditions. As a result, iridium tends to remain on the surface, exhibiting high OER activity of the SCIO-SG-P.[22–24] Finally, in the SCIO-SG sample [Fig. 3(c)], the O–H peak (531–532 eV) could be attributed to moisture absorption from the ambient environment, while the M–O peak near 529–530 eV reflects a strong lattice oxygen bonding with metal cations.[17,19] The observed decrease in hydroxide group intensity in SCIO-SG-P can be attributed to a transition toward an oxygen-deficient phase. This shift is further supported by the EDX elemental composition analysis of SCIO-SG and SCIO-SG-P, where the acid-leached samples showed an even lower oxygen content. Such a reduction in the oxygen content suggests that oxygen vacancies are formed in the iridium-rich phases. Consequently, the decrease in hydroxide groups is likely a direct result of these vacancies. They may have played a role in enhancing the efficiency of SCIO-SG-P. In addition, the structural defects and disorder introduced during leaching may lead to the formation of new oxygen states. These defects, particularly near metal cations that have transitioned to lower oxidation states (e.g., $Ir^{3+}/^{4+}$), can alter the local electronic environment of oxygen atoms. Consequently, the XPS spectrum of the post-processed sample might show a peak close to the carbonyl binding energy range, even in the absence of carbon, due to these newly formed oxygen species and the modified M–O bonding structure.

After physical and chemical characterizations, comprehensive electrochemical tests were carried out to evaluate the performance of SCIO as an OER catalyst. The initial cyclic voltammetry (CV) curves, normalized to the geometric surface area of the rotation disk electrode (RDE), are presented in Fig. 4(a), with the upper potential reaching 1.53 V vs the reversible hydrogen electrode (RHE). Different reduction–oxidation (redox) peaks of CV on SCIO before and after processing were observed in the first cycles, suggesting differences in the mechanisms of iridium reconstruction on the surface. The smaller but asymmetric redox pair in the range of 0.3–1.1 V vs RHE in the CV of the SCIO-SG is the sign of irreversible restructuring that can lead to the Sr and Co leaching and surface amorphization, as found in previous reports.[12,16,17] The single redox pair observed between 1.2 and 1.4 V for SCIO-SG suggests the presence of $Ir^{4+}/^{5+}$, which was identified by XPS of SCIO-SG, as shown in Fig. 3(a).[19] In contrast, the redox pairs in the CV of SCIO-SG-P are more symmetric, suggesting the reversible charge transfer and stable catalytic phase. The multiple redox pairs suggest the existence of $Ir^{3+}/^{4+}$ and $Ir^{4+}/^{5+}$ in SCIO-SG-P, as detected in the XPS spectra [Fig. 3(a)]. To understand how the redox peaks are associated with charge transfer and catalytic performance, Xu *et al.*[25] studied iridium oxide (IrO_x) catalysts in acidic OER using time-resolved *operando* spectroelectrochemistry and assigned three redox pairs to three key redox transitions of iridium. In their study, the first oxidative peak involves the oxidation of iridium from Ir^{3+} to $Ir^{3.x+}$ at ~0.9 V vs RHE, which prepares the iridium sites for active catalysis by initiating changes in the electronic environment. This stage is visible in CV as the onset of activity before the main catalytic current rise. The second oxidative peak progresses the oxidation state from $Ir^{3.x+}$ to Ir^{4+} around 1.3 V vs RHE, enhancing the catalytic activity essential for OER. This transition corresponds to increased currents in CV, indicating greater involvement in oxygen evolution. The third oxidative peak, occurring around 1.5 V vs RHE, further oxidizes Ir^{4+} to $Ir^{4.y+}$, fully activating the catalytic sites for oxygen evolution. This highest state is linked with the peak catalytic currents in CV, representing the most active phase for water oxidation. Similarly, three oxidative peaks at 0.7 and 1.2 V vs RHE in the CV of SCIO-SG-P were identified. Based on Bozal-Ginesta *et al.*'s[26] finding, iridium in SCIO-SG-P was predominantly reconstructed from Ir^{3+} to Ir^{4+} (~0.7 V) with a minor transition from Ir^{4+} to Ir^{5+} (~1.2 V), indicating the formation of surface Ir hydrous oxide (IrO_xH_y), which is believed to enhance catalytic efficiency. This assignment is supported by a prior study from Chen *et al.*,[17] who calculated using DFT to obtain a theoretical overpotential for H_2IrO_3 of 247 mV at 10 mA/cm^2_{geo}, which matches the overpotential observed for

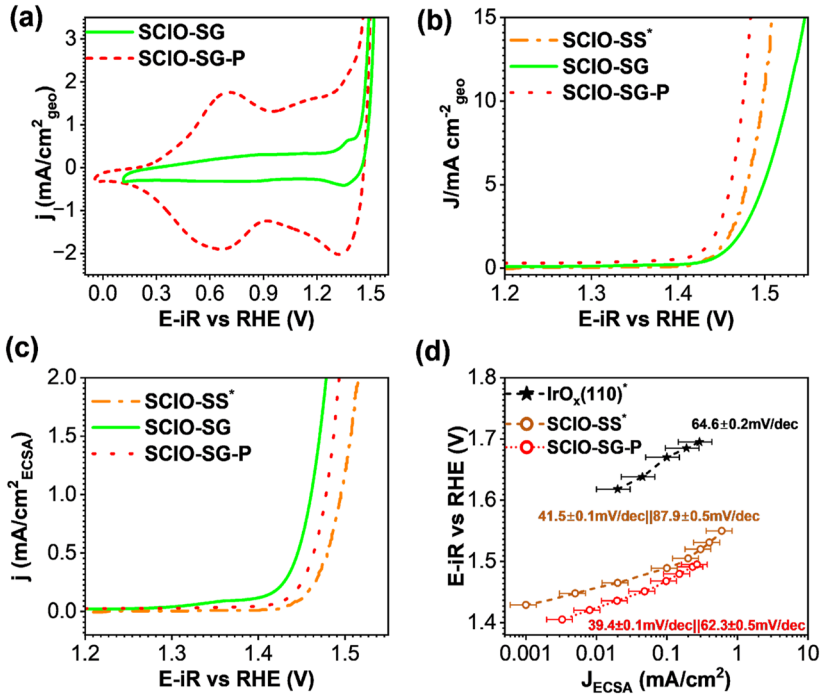

FIG. 4. (a) Initial cyclic voltammograms (CVs) of SCIO synthesized by the sol–gel method before the process (SCIO-SG) and SCIO synthesized by the sol–gel method after the process (SCIO-SG-P) with the upper potential reaching 1.53 V vs RHE. (b) iR-corrected OER polarization curves normalized to the geometric surface area of SCIO synthesized by the sol–gel method before the process (SCIO-SG) and SCIO synthesized by the sol–gel method after the process (SCIO-SG-P) compared to literature (denoted as * in the figure) from Chen *et al.* on solid state synthesized SCIO (SCIO-SS).[17] (c) iR-corrected OER polarization curves normalized to the Faradaic electrochemical surface area of SCIO synthesized by the sol–gel method before the process (SCIO-SG) and SCIO synthesized by the sol–gel method after the process (SCIO-SG-P) compared to the literature solid state synthesized SCIO (SCIO-SS).[17] (d) The corresponding Tafel slope of SCIO synthesized by the sol–gel method before the process (SCIO-SG) and SCIO synthesized by the sol–gel method after the process (SCIO-SG-P) compared to literature from Chen *et al.* on solid state synthesized SCIO (SCIO-SS) and IrO_x (110).[17]

SCIO-SG-P [245 mV at 10 mA/cm$^2_{geo}$, Fig. 4(b)], suggesting that a honeycomb H_2IrO_3 structure may dominate the surface. The consistency of redox pairs in CV measurements between our work and literature results further supports our post-synthesis treatment, which produces the final active SCIO phase that is similar to those obtained through electrochemical cycling and activation.[27,26]

Figures 4(b) and 4(c) compare the iR-corrected OER polarization curves for the SCIO-SG, SCIO-SG-P, and SCIO prepared via a solid-state method (SCIO-SS), tested under 0.1M $HClO_4$, with the current normalized to both the geometric surface area and electrochemically active surface area (ECSA). Note that both Faradaic and non-Faradaic ECSAs of SCIO were measured using CV (Fig. S10) and electrochemical impedance spectroscopy (EIS) (Fig. S9), respectively, with comparable values (~2.44 cm^2; see the supplementary material for more details). As shown in Fig. 4(b), when normalizing the exchange current to the geometric surface area, SCIO-SG-P exhibited the lowest overpotential (245 mV at 10 mA/cm$^2_{geo}$), namely the highest OER activity, compared to those of SCIO-SG (296 mV) and SCIO-SS (267 mV). Interestingly, when normalizing the current to the ECSA, SCIO-SG-P had a slightly lower OER activity (248 mV at 1 mA/cm$^2_{ECSA}$) compared to SCIO-SG (231 mV at 1 mA/cm$^2_{ECSA}$), but still showed better activity than SCIO-SS (255 mV at 1 mA/cm$^2_{ECSA}$). This is because the ECSA of SCIO-SG-P increased from the ball milling and acid leaching processes, giving 2.263 cm^2, which is approximately 20 times more than the ECSA of SCIO-SG, 0.11 cm^2 (Fig. S8), meaning more active surface sites participating in the reaction. The electrochemical performance of our SCIO samples was also compared with the commercial standard, TKK IrO_2, with all measurements performed in electrolytes with 1M proton concentration (Fig. S10), namely SCIO-SG and SCIO-SG-P in 1M $HClO_4$ and TKK IrO_2 in 0.5M H_2SO_4. SCIO-SG showed a worse and SCIO-SG-P exhibited a better OER activity (overpotential at 10 mA/cm$^2_{geo}$) compared to TKK IrO_2. Note that SCIO-SG-P has approximately the same performance (a minimal difference of only 24 mV at 10 mA/cm^2) in both 0.1 and 1M $HClO_4$ electrolytes (Fig. S11).

The Tafel slopes at 0.1M [H^+] of several catalysts are illustrated in Fig. 4(d). The SCIO-SG-P demonstrated good kinetics compared to all other OER catalyst references with the smallest Tafel slope (39.4 and 62.3 mV/dec). The similar Tafel slopes observed for the SCIO-SS after electrochemical activation and SCIO-SG-P within a similar potential range of 1.4–1.55 V suggest similarity of structure and composition of the final active SCIO phase. Under 1M [H^+], the Tafel slope of SCIO-SG-P after processing was 35.1 mV/dec between 1.3 and 1.45 V, which was better than the 49 mV/dec slope of TKK IrO_2 between 1.45 and 1.50 V, as shown in Fig. S9. With less iridium

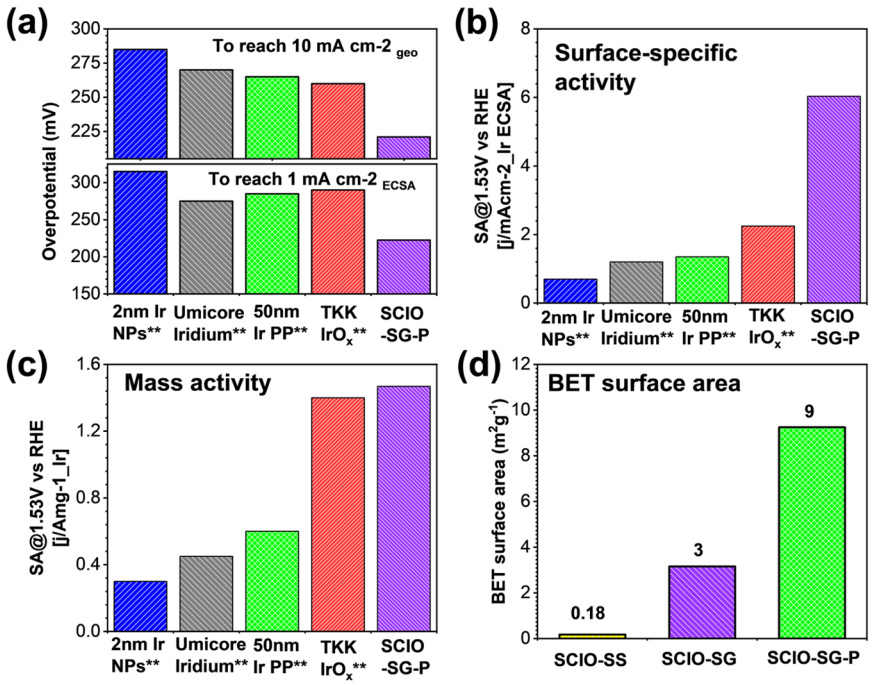

FIG. 5. (a) Overpotential comparison of some common commercialized OER catalysts (denoted as ** in the figure) from Tan *et al.* with sol–gel synthesized SCIO after processing (SCIO-SG-P).[20] (b) Initial surface-specific activities (SA) measured at 1.53 V vs RHE normalized to iridium ECSA of some common commercialized OER catalysts compared to sol–gel synthesized SCIO after processing (SCIO-SG-P).[20] (c) Initial mass activities (MA) measured at 1.53 V vs RHE normalized to mg iridium of some common commercialized OER catalysts compared to sol–gel synthesized SCIO after processing (SCIO-SG-P).[20] (d) BET surface area of sol–gel synthesized SCIO after processing (SCIO-SG-P) compared to sol–gel synthesized SCIO before processing (SCIO-SG-P) and solid-state synthesized SCIO.

usage, our sol–gel synthesized SCIO after post-synthesis treatment processes is more efficient.

To demonstrate the potential of our SCIO for commercialization, SCIO-SG-P was further tested in 1M $HClO_4$ and compared with other commercial standards, which were tested in 0.5M H_2SO_4 electrolytes and reported in the literature.[20] A more detailed future study could be needed since the anion species (ClO_4^- and SO_4^{2-}) can also influence OER.[28] As shown in Fig. 5(a), the SCIO-SG-P exhibited the smallest overpotential of 221 mV to reach 10 mA/cm^2_{geo} and 223 mV to reach 1 mA/cm^2_{ECSA}, indicating that SCIO-SG-P is the most effective in terms of both overall and intrinsic performance. At 1.53 V vs RHE, SCIO-SG-P achieved the highest current density of 6 mA/cm^2 per iridium ECSA, as shown in Fig. 5(b), compared to other standards. This led to the best mass activity among all commercial standards, as shown in Fig. 5(c). In particular, SCIO-SG-P has a higher mass activity of 1.47 $A/mg_{Ir\ ECSA}$ compared to the 1.4 $A/mg_{Ir\ ECSA}$ mass activity of TKK IrO_x at 1.53 V vs RHE when normalized to iridium loading, even though TKK IrO_x from Tan *et al.*[20] has ten times the BET surface area, further confirming the commercialization potential. Besides forming an active phase with Sr- and Co-deficiency and an amorphous structure, the enhanced OER performance of SCIO-SG-P is also due to the much-increased surface areas with more active sites exposed for SCIO-SG-P after post-synthesis treatment processes. As shown in Fig. 5(d), SCIO synthesized via the solid-state method has only a 0.18 m^2/g BET surface area, while the sol–gel synthesized SCIO exhibits a 3 m^2/g BET surface area. Following ball milling and acid leaching, the surface area further increased to 9 m^2/g (Fig. S13). The ball milling process likely contributed significantly to this increase in surface area, exposing more high-activity iridium on the SCIO surface, resulting in an enhanced OER performance compared to pristine SCIO. However, as shown in Fig. 2(d), SCIO particles are not uniform at the nanoscale after ball milling. Some are still micrometer sized. This indicates the potential for further size reduction to increase the surface area. However, when SCIO was ball milled for three days, the attempt to reduce particle size resulted in poor CV activity and powder dissociation, likely due to Sr and Co leaching out, which destabilized the catalyst (Fig. S1). This suggests that other methods should be considered for achieving tens of nanometers of SCIO. Another issue of SCIO catalysts is the stability. Although stability tests (Fig. S14, chronopotentiometric measurements at 10 mA/cm^2_{geo}) suggested a reasonably good performance of SCIO under less concentrated acidic conditions (0. 1M $HClO_4$) for an extended period (20.6 h at 1.49 V vs RHE), the catalyst cannot survive more than 1.6 h at 1M $HClO_4$. Further efforts should be devoted to improving SCIO long-term stability.

IV. CONCLUSIONS

In this study, the physical/chemical properties and electrochemical performance of $SrCo_{0.5}Ir_{0.5}O_3$ (SCIO) synthesized via the sol–gel method were systematically evaluated, with a particular focus on the effects of subsequent ball milling and acid leaching treatments on its OER activity. XRD and SEM results suggest the reduction in particle size from micrometers to ~460 nm and the formation of an amorphous structure after processes. EDX and XPS spectra confirm the Sr- and Co-deficiency and oxygen vacancies in the post-synthesis treated SCIO (SCIO-SG-P), matching the structure and composition of the active phase obtained from SCIO after electrochemical cycling (or activation). The CV results demonstrated that the SCIO-SG-P exhibited improved and stable OER activity

comparable to or even better than SCIO after electrochemical activation. Notably, SCIO-SG-P outperformed several Ir-based commercial catalysts in terms of OER activities. The SCIO-SG-P has a higher BET surface area of 9 m^2/g compared to both SCIO synthesized via solid-state methods (0.18 m^2/g) and before any processing (3 m^2/g). This substantial increase in the BET surface area is one critical factor for improving the catalytic performance, as a larger surface area allows more active sites to participate in the OER. The Tafel slope analysis confirmed superior OER kinetics, and stability tests indicated a reasonably good performance under less concentrated acidic conditions for an extended period. Our findings suggest that Ir-less SCIO as a highly active OER catalyst under acidic electrolyte conditions can be obtained through *ex-situ* physical and chemical processes without *in situ* electrochemical activation, which positions SCIO-SG-P as a very promising candidate for direct commercialization. Future efforts can be emphasized on the improvement of the catalytic stability of SCIO under acidic conditions. The development of this catalyst has contributed to the advancement of more robust and efficient OER catalysts, furthering the potential for sustainable hydrogen production technology.

SUPPLEMENTARY MATERIAL

The supplementary material provides detailed insights into the optimization processes for ball milling and acid leaching through cyclic voltammetry (CV) data, XRD pattern analyses, and particle size calculations. It includes SEM micrographs showing the effects of ball milling and acid leaching on particle size, nitrogen adsorption isotherms for surface area analysis, and EIS fittings for electrochemical surface area (ECSA) calculations. Additional data include comparisons of CV and Tafel slopes with IrO_2, stability tests at different electrolyte concentrations, and chronopotentiometry results demonstrating the catalyst's efficiency and durability under varying conditions.

ACKNOWLEDGMENTS

This work was supported by the National Science Foundation under Grant No. ITE-2236036. Part of this research was conducted at the Northwest Nanotechnology Infrastructure, a National Nanotechnology Coordinated Infrastructure site at Oregon State University, which was supported in part by the National Science Foundation (Grant No. NNCI-2025489) and Oregon State University. D. Y. also acknowledges Dr. Wei-Chi Lai for the useful discussions and suggestions on article writing.

AUTHOR DECLARATIONS

Conflict of Interest

The authors have no conflicts to disclose.

Author Contributions

Dongqi Yang: Conceptualization (supporting); Data curation (lead); Formal analysis (lead); Investigation (equal); Methodology (equal); Validation (equal); Writing – original draft (lead). **Nicolai Andreas**: Formal analysis (supporting); Validation (supporting). **Ankit K. Yadav**: Formal analysis (supporting). **Kyriakos C. Stylianou**: Writing – review & editing (supporting). **Zhenxing Feng**: Conceptualization (lead); Funding acquisition (lead); Investigation (lead); Methodology (lead); Project administration (lead); Resources (lead); Supervision (lead); Validation (lead); Writing – review & editing (lead).

DATA AVAILABILITY

The data that support the findings of this study are available within the article and its supplementary material.

REFERENCES

[1] J. A. Turner, Science **124**, 345 (1956).
[2] J. Andrews and B. Shabani, Int. J. Hydrogen Energy **37**(2), 1184–1203 (2012).
[3] P. P. Edwards, V. L. Kuznetsov, W. I. David, and N. P. Brandon, Energy Policy **36**(12), 4356–4362 (2008).
[4] M. Conte, A. Iacobazzi, M. Ronchetti, and R. Vellone, J. Power Sources **100**(1–2), 171–187 (2001).
[5] Ö. F. Selamet, F. Becerikli, M. D. Mat, and Y. Kaplan, Int. J. Hydrogen Energy **36**(17), 11480–11487 (2011).
[6] F. Barbir, Sol. Energy **78**(5), 661–669 (2005).
[7] E. Brightman, J. Dodwell, N. van Dijk, and G. Hinds, Electrochem. Commun. **52**, 1–4 (2015).
[8] M. T. Dinh Nguyen, A. Ranjbari, L. Catala, F. Brisset, P. Millet, and A. Aukauloo, Coord. Chem. Rev. **256**(21–22), 2435–2444 (2012).
[9] G. Brändle, M. Schönfisch, and S. Schulte, Appl. Energy **302**, 117481 (2021).
[10] Z. Chen, L. Guo, L. Pan, T. Yan, Z. He, Y. Li, C. Shi, Z. F. Huang, X. Zhang, and J. J. Zou, Adv. Energy Mater. **12**(14), 2103670 (2022).
[11] Y. Lee, J. Suntivich, K. J. May, E. E. Perry, and Y. Shao-Horn, J. Phys. Chem. Lett. **3**(3), 399–404 (2012).
[12] L. C. Seitz, C. F. Dickens, K. Nishio, Y. Hikita, J. Montoya, A. Doyle, C. Kirk, A. Vojvodic, H. Y. Hwang, J. K. Norskov, and T. F. Jaramillo, Science **353**(6303), 1011–1014 (2016).
[13] E. Antolini, ACS Catal. **4**(5), 1426–1440 (2014).
[14] S. B. Scott, J. E. Sørensen, R. R. Rao, C. Moon, J. Kibsgaard, Y. Shao-Horn, and I. Chorkendorff, Energy Environ. Sci. **15**(5), 1988–2001 (2022).
[15] S. Cherevko, S. Geiger, O. Kasian, N. Kulyk, J.-P. Grote, A. Savan, B. R. Shrestha, S. Merzlikin, B. Breitbach, A. Ludwig, and K. J. Mayrhofer, Catal. Today **262**, 170–180 (2016).
[16] G. Wan, J. W. Freeland, J. Kloppenburg, G. Petretto, J. N. Nelson, D. Y. Kuo, C. J. Sun, J. Wen, J. T. Diulus, G. S. Herman, Y. Dong, R. Kou, J. Sun, S. Chen, K. M. Shen, D. G. Schlom, G. M. Rignanese, G. Hautier, D. D. Fong, Z. Feng *et al.*, Sci. Adv. **7**, eabc7323 (2021).
[17] Y. Chen, Y. Sun, M. Wang, J. Wang, H. Li, S. Xi, C. Wei, P. Xi, G. E. Sterbinsky, J. W. Freeland *et al.*, Sci. Adv. **7**(50), eabk1788 (2021).
[18] E. Fabbri, A. Habereder, K. Waltar, R. Kotz, and T. J. Schmidt, Catal. Sci. Technol. **4**(11), 3800–3821 (2014).
[19] Y. Chen, H. Li, J. Wang, Y. Du, S. Xi, Y. Sun, M. Sherburne, J. W. Ager, III, A. C. Fisher, and Z. J. Xu, Nat. Commun. **10**(1), 572 (2019).
[20] X. Tan, J. Shen, N. Semagina, and M. Secanell, J. Catal. **371**, 57–70 (2019).
[21] S. Brunauer, P. H. Emmett, and E. Teller, J. Am. Chem. Soc. **60**(2), 309–319 (1938).
[22] K. S. W. Sing, D. H. Everett, R. A. W. Haul, L. Moscou, R. A. Pierotti, J. Rouquerol, and T. Siemieniewska, Pure Appl. Chem. **57**, 603–619 (1985).

[23]B. Weber, in *Coordination Chemistry*, edited by W. Birgit (Springer Spektrum, Berlin, Heidelberg, 2023), pp. 87–105.
[24]M. Retuerto, L. Pascual, O. Piqué, P. Kayser, M. A. Salam, M. Mokhtar, J. A. Alonso, M. Peña, F. Calle-Vallejo, and S. Rojas, J. Mater. Chem. A **9**(5), 2980–2990 (2021).
[25]J. Xu, S. Qin, C. Zheng, J. Wang, B. Yang, G. Qiu, S. Cui, and H. Ma, JOM **75**(12), 5785–5795 (2023).
[26]C. Bozal-Ginesta, R. R. Rao, C. A. Mesa, X. Liu, S. A. J. Hillman, I. E. L. Stephens, and J. R. Durrant, ACS Catal. **11**(24), 15013–15025 (2021).
[27]M. Yu, K. S. Belthle, C. Tüysüz, and H. Tüysüz, J. Mater. Chem. A **7**(40), 23130–23139 (2019).
[28]G. A. Kamat, J. A. Zamora Zeledón, G. T. K. K. Gunasooriya, S. M. Dull, J. T. Perryman, J. K. Nørskov, M. B. Stevens, and T. F. Jaramillo, Commun. Chem. **5**, 20 (2022).